2-6-2019

Thermally Induced Disorder-Order Phase Transition of Gd 2 Hf 2 O 7 :Eu 3+ Nanoparticles and its Implication on Photo-and Radioluminescence

Santosh K. Gupta

Maya Abdou

Partha Sarathi Ghosh

Jose P. Zuniga

Yuanbing Mao
The University of Texas Rio Grande Valley, yuanbing.mao@utrgv.edu

ACS OMEGA

Article

Cite This: ACS Omega 2019, 4, 2779−2791

http://pubs.acs.org/journal/acsodf

Thermally Induced Disorder−Order Phase Transition of $Gd_2Hf_2O_7:Eu^{3+}$ Nanoparticles and Its Implication on Photo- and Radioluminescence

Santosh K. Gupta,[†,‡] Maya Abdou,[†] Partha Sarathi Ghosh,[§] Jose P. Zuniga,[†] and Yuanbing Mao*[,†,∥]

[†]Department of Chemistry and [∥]School of Earth, Environmental, and Marine Sciences, University of Texas Rio Grande Valley, 1201 West University Drive, Edinburg, Texas 78539, United States

[‡]Radiochemistry Division and [§]Materials Science Division, Bhabha Atomic Research Centre, Trombay, Mumbai 400085, India

Supporting Information

ABSTRACT: Crystal structure has a strong influence on the luminescence properties of lanthanide-doped materials. In this work, we have investigated the thermally induced structural transition in $Gd_2Hf_2O_7$ (GHO) using Eu^{3+} ions as the spectroscopic probe. It was found that complete phase transition from the disordered fluorite phase (DFP) to the ordered pyrochlore phase (OPP) can be achieved in GHO with the increase of annealing temperature from 650 → 1100 → 1300 °C. OPP is the more stable structural form for the GHOE nanoparticles (NPs) annealed at a higher temperature based on the energy calculation by density functional theory (DFT). The asymmetry ratio of the GHOE-650 NPs was the highest, whereas the quantum yield, luminescence intensity, and lifetime values of the GHOE-1300 NPs were the highest. Emission intensity of Eu^{3+} ions increases significantly with the phase transition from the DFP to OPP phase and is attributed to the higher radiative transition rate (281 s^{-1}) of the $^5D_0$ level of the Eu^{3+} ion in the environment with relatively lower symmetry (C_{2v}) because of the increase of crystal size. As the structure changes from DFP to OPP, radioluminescence showed tunable color change from red to orange. The Eu^{3+} local structure obtained from DFT calculation confirmed the absence of inversion symmetry in the DFP structure, which is consistent with the experimental emission spectra and Stark components. We also elucidated the host to dopant optical energy transfer through density of states calculations. Overall, our current studies present important observations for the GHOE NPs: (i) thermally induced order−disorder phase transition, (ii) change of point group symmetry around Eu^{3+} ions in the two phases, (iii) high thermal stability, and (iv) tunability of radioluminescent color. This work provides fundamental understanding of the relationship between the crystal structure and photophysical properties of lanthanide-doped materials and helps design a strategy for advanced optoelectronic materials.

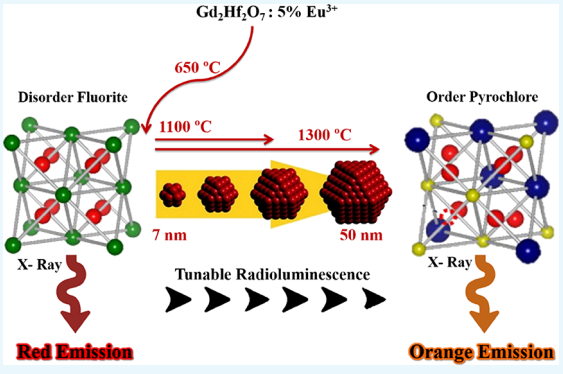

1. INTRODUCTION

Materials with $A_2B_2O_7$ composition belonging to the pyrochlore group have been the focal point of research in the scientific community for the past few decades owing to their various interesting properties such as low thermal conductivity, high dielectric constant, suitable refractive index, high structural stability, high radiation stability, and so forth. These properties enable them to be suitable for many applications such as catalysis,[1] phosphor,[2] nuclear waste host,[3] scintillator,[2,4] defect fluorescence,[5] magnetism,[6] thermal barrier coatings,[7] and sensors.[8] They are known to exist in two structural variants: ordered pyrochlore (OP, $Fd\bar{3}m$) and disordered fluorite (DF, $Fm\bar{3}m$). OP is structurally very close to DF, except it has two cationic sites, three anionic sites located at 48f (O_a), 8a (O_b), and 8b (O_c) Wyckoff positions, and 1/8th of oxygen ions at the 8b site are missing. Hence, they are considered as similar phases but with different degrees of anion and cation ordering. The phase transition is normally induced by chemical doping,[9] pressure,[10] temperature,[11] irradiation,[12] and so forth. The ionic radius ratio (IRR) plays an important role in the structural phase transition of DF ⇄ OP. It is reported that the OP phase is stable when the IRR value is greater than 1.46, while the DF phase is the more stable phase when the IRR value is below 1.46.[13] Some of the complex $A_2B_2O_7$ oxides fall in the "boundary" region with IRR ∼1.46, where they can have the DF structure or the OP structure depending on the synthesis conditions adopted.

Among various $A_2B_2O_7$ compounds, $Gd_2Hf_2O_7$ (GHO) stands out owing to its interesting properties such as high dielectric constant, wide temperature range of phase stability, and high melting point, which gives GHO broad application

Received: December 10, 2018
Accepted: January 17, 2019
Published: February 6, 2019

DOI: 10.1021/acsomega.8b03458
ACS Omega 2019, 4, 2779−2791

potentials as magnetic materials,[14,15] high dielectric constant materials,[16] high-temperature ceramics, solid electrolyte in solid oxide fuel cells,[17] and thermal barrier coatings.[18] GHO has a cubic structure as well as high Z_{eff}, making it a potential host lattice for scintillators.[19,20] Moreover, given its high melting point and high structural and thermal stabilities, it can be a potential host for lanthanide ion-doped phosphor. The IRR of GHO is approximately around 1.48 (close to 1.46),[21] so it is expected that the DF and OP phases can coexist in GHO depending on the synthesis conditions.

Recently, many studies have revealed that precise architectural manipulation of nanomaterials have fetched lots of scientific attention because the properties of nanocrystals depend strongly on shape, size, and structure.[22] It is reported that when GHO is synthesized at a nanodomain, it can undergo DF to OP phase transition at temperatures above 1300 °C.[13] The phase transition proceeds via formation of the pyrochlore nanoparticles (NPs) in the matrix of well-crystallized fluorite. Therefore, it becomes imperative to probe the structural phase transition and its influence on the luminescence properties of GHO from the perspective of using it as a host for other lanthanide-based phosphors and scintillators. Recently, it was found that the crystal structure plays a very important role in designing efficient luminescent materials. The hexagonal structure of GdF_3:Eu^{3+} was found to be more efficient phosphor than its orthorhombic counterpart.[22] Similarly, hexagonal EuF_3 is more efficient luminescent material compared to orthorhombic EuF_3.[23] There is very scarce literature collection on the optical properties of GHO pyrochlore. Previously, Papan et al. have carried out luminescence spectroscopy and Judd−Ofelt analysis on the combustion-synthesized europium-doped $Y_2Hf_2O_7$, GHO, and $Lu_2Hf_2O_7$.[24] Our group has also investigated the effect of A-site ions on the structural and optical properties of a series of europium-doped rare-earth hafnate $RE_2Hf_2O_7$ NPs (RE = Y, La, Pr, Gd, Er, Lu).[25] There have been few work on luminescence properties of europium ion-doped gadolinium-based pyrochlores, such as zirconate, titanate, and stannate, wherein fundamental photophysical properties of Eu^{3+}, its symmetry, and red-emitting phosphor applications have been discussed.[26−29] Zhang et al. observed high intensity of $^5D_0 \rightarrow {}^7F_1$ transition than that of $^5D_0 \rightarrow {}^7F_2$ transition.[30] Their group has also investigated the effect of codoping V^{5+} ions on an orange/red emission ratio of $Gd_2Ti_2O_7$:Eu^{3+} phosphor. Liao et al. have investigated a similar trend which indicated a local symmetry of the Eu^{3+} ion in the GSO crystal lattice has an inversion center of the Gd^{3+} ion with the D_{3d} point group.[31] None of the reported work investigated the thermally induced disorder−order phase transition and its effect on photo- and radioluminescence properties of lanthanide-doped GHO NPs for possible applications in UV-based phosphors and scintillators.

Temperature is an important physical parameter that can alter lattice spacing and modify the band and therefore the electronic properties of various materials. By executing high-temperature annealing, one can modulate the structures, create novel properties, and bring out the phenomena not observed at ambient conditions.[32−34] Thermally induced structural phase transition of pyrochlore NPs would be expected to unravel various interesting optical properties. Therefore, it is of great interest to explore the disorder−order phase transition and luminescence properties of nanosized GHOE under various annealing temperatures. Up until now, there has been no report about the thermally induced structural transition and its implication on photo- and radioluminescence (RL) properties of nanosized GHOE. The studies on the high-temperature annealing of nanosized GHOE would be of great significance not only to fundamental and applied research but also would give new insights into the nature of the $A_2B_2O_7$ system.

In this study, we have first synthesized GHO NPs using a molten-salt synthesis (MSS) method at a relatively low temperature of 650 °C. We have doped 5.0% of trivalent europium ions into GHO (GHOE) with the aim of exploring GHO as a host for phosphors and scintillators, which has never been reported before. A europium ion is selected because its electronic transitions are strongly affected by the structural change, coordination number, crystal field, and so forth. We correlated the change of its photoluminescence (PL) properties as GHO undergoes the DF phase (DFP) → OP phase (OPP) phase transition using europium ions as a spectroscopic probe.[35] Because DFP has a disordered array of cations/anions, whereas the opposite prevails in OPP, structural changes could be easily identified based on PL properties such as asymmetry ratio, Stark splitting, and lifetime of europium ions. The goals of this work include the synthesis of GHOE with the DFP structure at low temperature using our MSS procedure, the investigation of thermally induced structural phase transition and its implication on the photo- and radioluminescence properties of GHOE, and the determination of various optical parameters for the GHOE samples. Therefore, our work does not only exploit the potential of this interesting material as light-emitting phosphor and scintillator but also unveils a phase-dependent design strategy to develop materials with desirable properties. We have also explored the thermal stability of GHOE NPs for possible application in thermal sensors and high-temperature luminescence.

The phase transition from DF to OP at high temperature is further supported by density functional theory (DFT)-calculated cohesive energies of both GHO and GHOE. DFT calculations were performed to study the relative phase stability of DF and OP phases of both GHO and GHOE. DFT calculation results were used to bring out the structure−PL correlation by explaining the origin of intense hypersensitive electric dipole transition (EDT) and large spectral splitting. The complete host to europium energy transfer is also explained using density of state (DOS) calculations for both GHO and GHOE.

2. RESULTS AND DISCUSSION

2.1. Structural Characterization by X-ray Diffraction, Raman Spectroscopy, and Scanning Electron Microscopy. Figure S1 shows the X-ray diffraction (XRD) patterns of the GHO-650, GHOE-650, GHOE-1100, and GHOE-1300 NPs to see any kind of phase transition or structural evolution. All patterns and the corresponding 2θ and hkl values are in agreement with DFP,[18] which reveals that all of the GHO and GHOE NPs are single phased with the $Fm\bar{3}m$ space group. There is no evidence of the diffraction peak corresponding to the pyrochlore phase (space group $Fd\bar{3}m$), which is characterized by the occurrence of superlattice reflections with 2θ at 29°, 37°, and 44.7°. It is reported that the formation of the OP completes at an annealing temperature of ∼1000−1200 °C for 3 h, and the pyrochlore phase is detected by diffraction techniques.[13] In another work, Popov et al. have also observed the formation of the OP structure from GHO NPs at 1200−1300 °C.[36−38] However, our XRD results do not reveal the OP phase even from the GHOE-1300 NPs. Because of the closeness of the atomic

DOI: 10.1021/acsomega.8b03458
ACS Omega 2019, 4, 2779−2791

numbers of gadolinium (Z = 64) and hafnium (Z = 72), the superstructure reflections are too small to be observed by nonresonant diffraction studies to confirm the formation of the long-range cationic order of the pyrochlore phase.[38]

As can be seen from Table 1, there is a proportional increase in crystalline size of the GHOE NPs as a function of annealing temperature. This can also be seen from the narrowing of the XRD peaks at a higher annealing temperature. Moreover, the doping of the europium ion does not distort the basic structural network of GHO.

Table 1. Lattice Parameter and Crystallite Size of the GHO and GHOE NPs

sample	2θ (deg)	FWHM (β)	lattice parameters (Å)	crystal size (nm)
GHO-650	29.58	1.06	10.45	7.49
GHOE-650	29.74	1.03	10.39	7.71
GHOE-1100	29.72	0.22	10.40	36.11
GHOE-1300	29.66	0.16	10.43	49.65

Figure 1a shows the Raman spectra of the GHO-650, GHOE-650, GHOE-1100, and GHOE-1300 NPs. Raman spectroscopy is one of the most sought out techniques to differentiate the OP and DF phases of $A_2B_2O_7$ compounds, which is difficult to achieve using XRD. It is well documented in the literature based on the group theory that there are a total of six Raman active vibrational modes existing in the wavenumber range of 200−1000 cm^{-1} for the OP phase, which are $\Gamma_{OP} = A_{1g} + E_g + 4F_{2g}$.[39,40] On the other hand, because seven O^{2-} ions are randomly oriented over the eight anionic sites leading to high level of structural disordering, the DF phase has mainly one active Raman mode F_{2g}. Phase transition from the $A_2B_2O_6O'$ P ($Fm\bar{3}m$ space group, Z = 8) to perfect AO_2 F ($Fd\bar{3}m$, Z = 4) structure proceeds by disappearance of A_{1g} and E_g Raman modes and decrease in the number of F_{2g} modes from 4 to 1. IRR (r_A/r_B) plays an important role in determining the type of structure which $A_2B_2O_7$ composition is going to attain.[41] It is reported that if IRR is less than 1.46, the DF phase is more likely to form and if it exceeds 1.46, it is the OP phase, which is more likely to be stabilized at room temperature. As discussed earlier, GHO exists in the phase boundary of OP ⇔ DF phase transition as its IRR value is 1.48.

The Raman spectrum of the GHO-650 NPs (Figure 1a) consists of a single broad peak characteristic of the DF phase. Moreover, europium-doped GHOE-650 NPs also exist in the DF phase, which indicates that europium doping does not change the basic fluorite network of GHO. However, after the GHOE-650 NPs are annealed at 1100 and 1300 °C, there is an induction of pyrochlore ordering in the GHOE NPs. There is an evolution of pyrochlore peaks at 1100 °C, which completely transform to the OP structure at 1300 °C. From the Raman spectra, we could clearly identify six vibrational modes related to Gd−O and Hf−O vibrational frequencies of the GHOE-1100 NPs. The peak positions are approximately around 306, 321, 401, 500, 520, and 640 cm^{-1}, which correspond to F_{2g}, E_g, F_{2g}, A_{1g}, F_{2g}, and F_{2g}, respectively.[42] The vibrational Raman bands of F_{2g}, E_g, and F_{2g} modes at a lower wavenumber region (300−400 cm^{-1}) originate from vibrations of the La−O and Hf−O bonds, whereas the F_{2g} band at higher wavenumber (520 and 640 cm^{-1}) comes into picture because of the stretching of the Hf−O bonds. The Gaussian deconvoluted Raman spectrum of the GHOE-1300 NPs possessing an ideal pyrochlore structure is shown in Figure S2.

The observed change in phase $Fm\bar{3}m \rightarrow Fd\bar{3}m$ of the GHOE NPs is in line with the Ostwald's step rule,[38] as it is reported that the OP structure in GHO has a low enthalpy of formation compared to the DF structure.[43] The activation energy (E_a) of the thermal growth of the GHO NPs with the DF structure was 65 kJ/mol in the temperature range of 800−1400 °C.

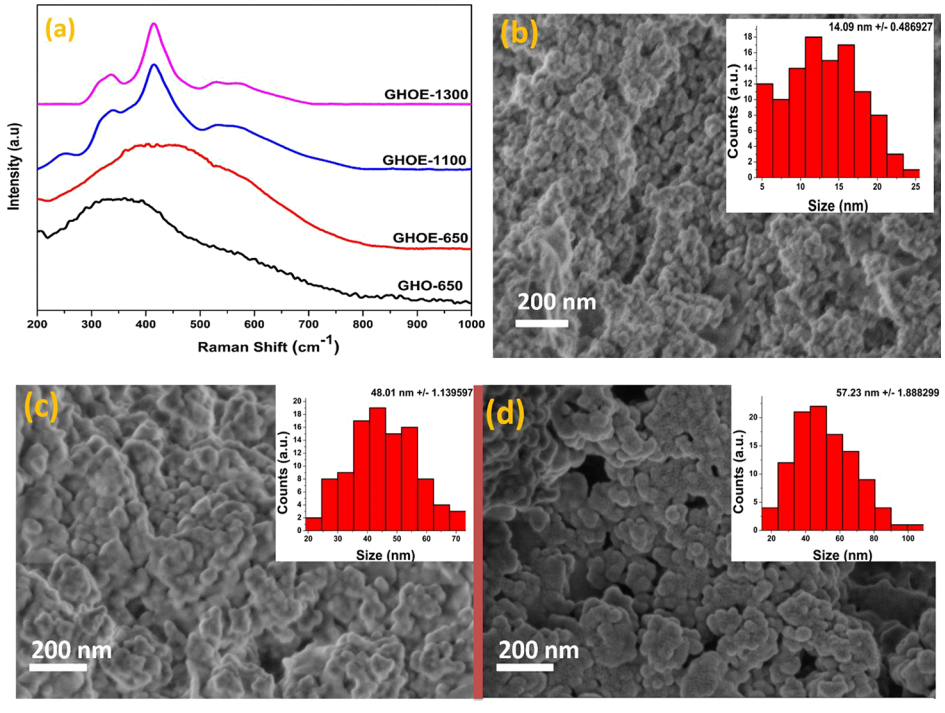

Figure 1. (a) Raman spectra of the GHO-650, GHOE-650, GHOE-1100, and GHOE-1300 NPs. SEM images of the (b) GHOE-650, (c) GHOE-1100, and (d) GHOE-1300 NPs.

DOI: 10.1021/acsomega.8b03458
ACS Omega 2019, 4, 2779−2791

Table 2. DFT-GGA Calculated Equilibrium Lattice Parameters, Atomic Positions, Bond Lengths, and Band Gap of GHO in the OP Structure are Summarized in This Table along with Previous Experimental Measurements and Theoretical Calculations

	a_0 (Å)	X	Gd−O_{8b} (Å)	Gd−O_{48f} (Å)	Hf−O_{48f} (Å)	band gap (eV)
this study GGA	10.59	0.34	2.29	2.56	2.08	3.45
previous GGA[44]	10.53	0.34	2.28	2.53	2.07	3.42
experiment[38]	10.52					

Scanning electron microscopy (SEM) images (Figure 1b−d) show that the GHOE-650, GHOE-1100, and GHOE-1300 NPs are either spheroidal or spherical and have certain degree of agglomeration. The particle size distribution of the GHOE NPs was calculated from these SEM images by ImageJ software as shown in the insets. There is a progressing increase of the average particle size of these GHOE NPs, that is 14 nm of the GHOE-650 NPs, 48 nm of the GHOE-1100 NPs, and 57 nm of the GHOE-1300 NPs.

2.2. Cohesive Energies of OP and DF Structures: A DFT Study. The DFT-generalized gradient approximation (GGA)-calculated equilibrium lattice parameters, atomic positions, and bond lengths are summarized in Table 2 along with previous DFT calculation results.[44] Table 2 clearly shows that our values calculated via GGA−Perdew−Burke−Ernzerhof agree well with previous GGA−PW91 calculated values and GGA is sufficient to reproduce the insulating character of GHO. The lattice constant (a_o), the internal structural parameter (x) which is related to the position of O_{48f}, the nearest Gd−O_{8b}, Gd−O_{48f}, and Hf−O_{48f} distances and the band gap are tabulated in Table 2.

Table 3 shows our DFT-GGA-calculated cohesive energies of OP and DF structures of GHO, and the OP structure is stable

Table 3. DFT-GGA-Calculated Cohesive Energies of OP and DF Structures of the GHO and GHOE NPs Tabulated with Respect to the Most Stable Structure[a]

system	GHO (eV)	GHOE (eV)
OP	0.00	Gd site: 6.127, Hf site: 0.000
DF	8.177	Gd site: 10.407, Hf site: 9.666

[a]The different energy values are reported for the 88-atom supercell.

with respect to DF. In the bulk state, the OP structure is favorable with respect to the DF structure. Moreover, Jiang et al.[45] and Li et al.[46] have shown that the ground state structure of GHO is OP. They have also calculated OP to DF transformation temperatures for several pyrochlores. Therefore, our DFT results are in agreement with previous DFT calculation results. Further, our DFT-GGA results show that with Eu doping (1 Eu atom in the 88-atom supercell), the OP structure is stable with respect to the DF.

Our experimental results show that the crystallite size increases with increasing annealing temperature (Table 1). Increasing crystallite size implies lower surface to volume ratio with approaching bulk characteristics. The crystallite size of the GHOE-650 NPs is around 7.0 nm, whereas that of the GHOE-1300 NPs is ∼50 nm. Raman spectra of the GHOE-1100 and GHOE-1300 NPs confirm the formation of the OP structure. Therefore, the OP structure is favorable in the GHO and GHOE NPs after high-temperature annealing and corroborating with our calculated DFT energetics shown in Table 3.

2.3. Local Site Stability of Eu^{3+} Ions in the GHOE NPs. Figure 2 shows the DFT-GGA-calculated distribution of Gd−O, Hf−O, and Eu−O bond lengths in the DF structure with Eu doped at the Gd site (Figure 2a) and the Hf site (Figure 2b). The

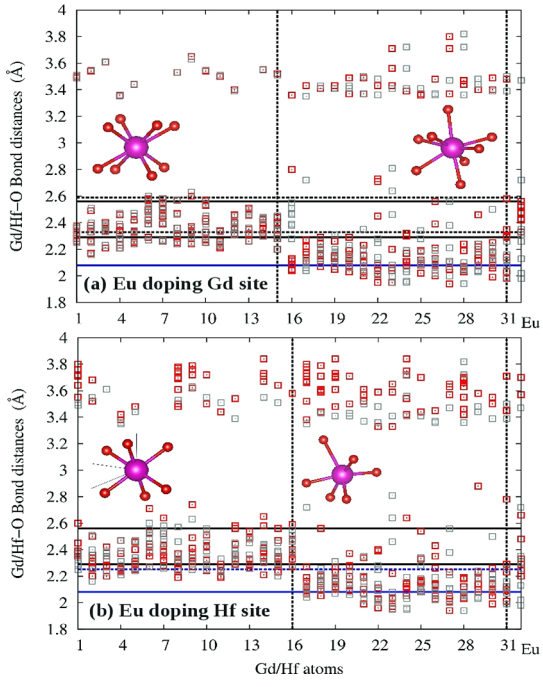

Figure 2. DFT-GGA-calculated Gd−O, Hf−O, Eu−O, and Gd−Gd/Hf bond length distributions of each Gd/Hf/Eu atom in the DF structure: (a) Eu-doping Gd site and (b) Eu-doping Hf site. Solid black (blue) lines show Gd−O (Hf−O) bond distances in the OP structure. Dotted black/blue lines show Eu−O bond distances in the OP structure. The configuration of EuO_8/EuO_6 polyhedra when doped in OP (DF) is shown in the left (right) side of the figure.

solid black lines (at 2.29 and 2.56 Å) and dotted black lines (at 2.33 and 2.59 Å) show our DFT-GGA-calculated Gd−O and Eu−O (Eu doped at the Gd site) bond lengths in the OP structure, respectively. Similarly, a solid blue line (at 2.08 Å) and a dotted blue line (at 2.25 Å) show our DFT-GGA-calculated Hf−O and Eu−O (Eu doped in the Hf site) bond lengths in the OP structure, respectively. The x-axis of the figures shows Gd atoms (1st−15/16th), Hf atoms (15/16th−31st), and a Eu atom (32nd) in 88-atom special quasirandom structure DF. The red and gray points show bond lengths of Eu-doped and -undoped DF GHO, respectively. This means that in the 88-atom supercell, there are 16 Gd atoms, 16 Hf atoms, and 56 oxygen atoms. If Eu is doped in the Gd site, then in the supercell, 1st 15 atoms are Gd, next 16 atoms are Hf, and the 32nd atom is Eu. Similarly, if doped at the Hf site, then in the supercell, 1st 16 atoms are Gd, next 15 atoms are Hf, and the 32nd atom is Eu.

The bond lengths in EuO_8 polyhedra in OP are 2.33 (2 bonds) and 2.59 Å (6 bonds) which is ∼2% higher (2.29 and 2.56 Å) compared to those of GdO_8 polyhedra. The Eu−O bond lengths are ∼8.2% higher in EuO_6 polyhedra compared to that of HfO_6. Moreover, our DFT-GGA calculated energetics shows that Eu doped at the Hf site is favorable compared to the Gd site, and the energy difference is 6.13 eV in the OP structure. In the DF structure, Gd−O bond distances are distributed over the

DOI: 10.1021/acsomega.8b03458
ACS Omega 2019, 4, 2779−2791

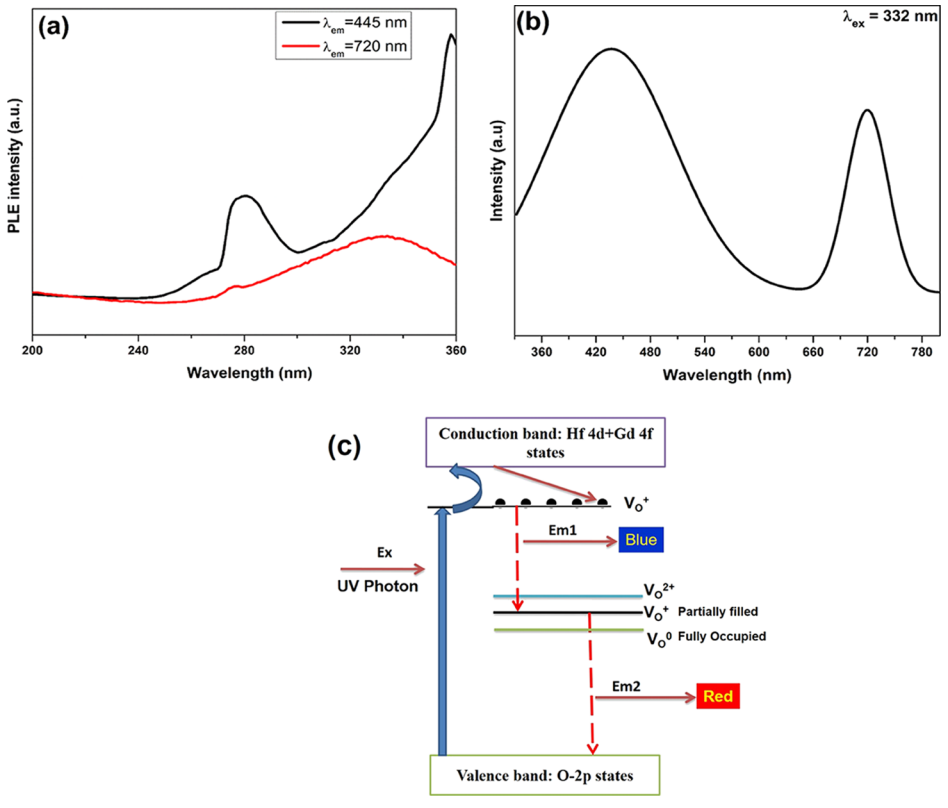

Figure 3. (a) Excitation spectra, (b) emission spectrum, and (c) proposed mechanism of the blue and red emissions of the GHO-650 NPs.

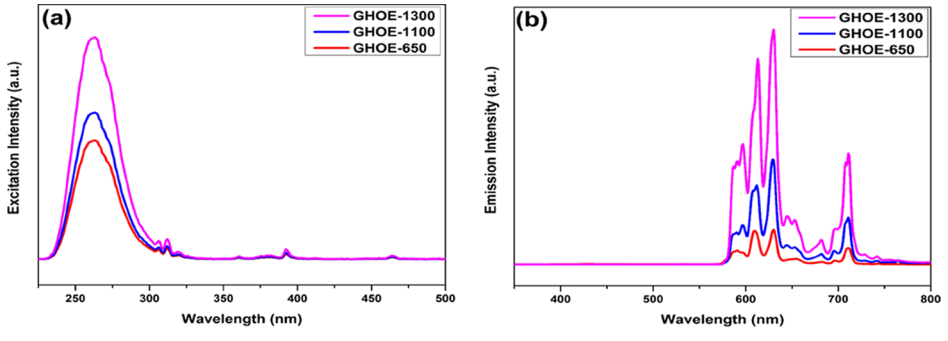

Figure 4. (a) PL excitation spectra (λ_{em} = 612 nm) (b) PL emission spectra (λ_{ex} = 263 nm) for GHOE NPs.

range of 2.16−2.60 Å in the form of GdO_6, GdO_7, and GdO_8 polyhedra. The Hf−O bond distances are distributed over the range of 1.94−2.81 Å in the form of HfO_6 and HfO_7 polyhedra. The Hf−O bond distances are distributed in a wide range compared to an OP HfO_6 bond length of 2.08 Å. In other words, the chemical environment around the Hf site is more distorted compared to that of Gd.

Figure 2 also shows the change in the first and second nearest neighbor bond distances because of Eu doping at Gd and Hf sites. The Gd−Gd/Hf bond lengths change appreciably by Eu doping at the Hf site compared to Eu doping at the Gd site. Moreover, our DFT-GGA-calculated energetics shows that Eu doping in the Hf site is favorable compared to the Gd site, and the energy difference is 0.74 eV. In addition, Figure 2 shows EuO_8 (doped at the Gd site) and EuO_6 (doped at the Hf site) polyhedra in OP (shown on the left) and DF (shown on the right) structures. The distribution of bond lengths and orientation shows that EuO_8 and EuO_6 polyhedra has inversion symmetry when doped in the OP structure and inversion symmetry is absent when doped in the DF structure. The emission spectra from different excitation wavelengths and number of Stark components of the $^5D_0 \rightarrow {}^7F_J$ (J = 0−4) transitions of the Eu^{3+} ion in the GHOE-650 NPs (Figures S3b and 5) show that Eu atoms occupy a chemical environment in the DF structure which has no inversion symmetry. These results are consistent with our DFT-calculated results of the local structure around Eu atoms, which also confirm the absence of inversion symmetry.

2.4. PL Properties of the GHO-650 NPs. Figure 3a,b show the PL excitation spectra and the emission spectrum of GHO-650 NPs, respectively. The emission spectrum displayed two emission maxima at ∼445 and 720 nm corresponding to blue and red emissions, respectively. Such display of multicolor emissions (blue and red in this case) is a characteristic of nanomaterials wherein the excited state dissipates its excessive energy through various channels because of large number of defect states within band gaps of nanomaterials.[47] It is known that $A_2B_2O_7$ pyrochlore type ceramics are rich in defects and

DOI: 10.1021/acsomega.8b03458
ACS Omega 2019, 4, 2779−2791

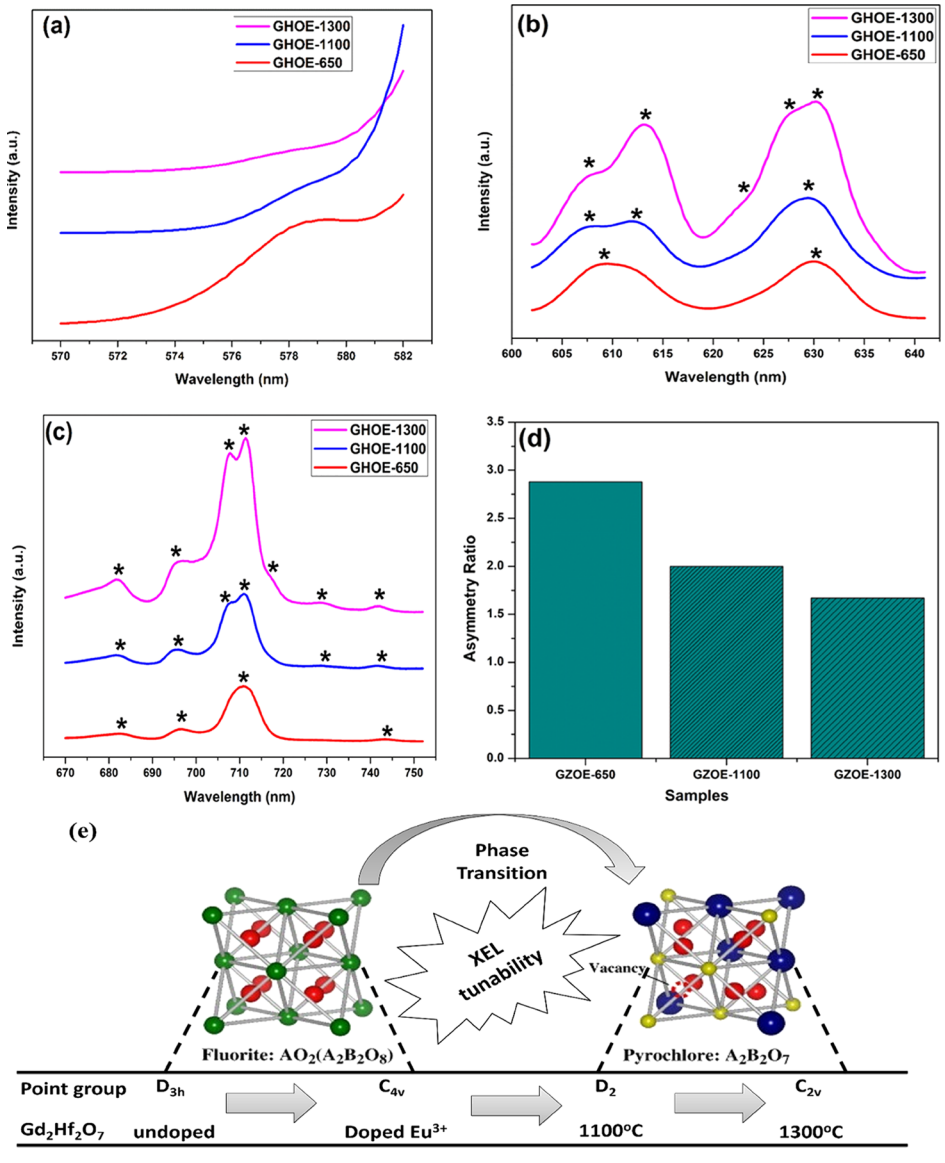

Figure 5. Stark-splitting patterns of the (a) $^5D_0 \rightarrow {}^7F_0$, (b) $^5D_0 \rightarrow {}^7F_2$, and (c) $^5D_0 \rightarrow {}^7F_4$ transitions; (d) asymmetry ratio of the GHOE samples; and (e) schematic of the effect of annealing temperature on structural change of the GHO host and the point group symmetry of Eu^{3+} dopants. X-ray excited luminescence is abbreviated as XEL.

more so in oxygen vacancies.[48] The Raman spectrum of the GHO-650 NPs (Figure 1a) indicated that it exists in the DF phase with large concentration of oxygen vacancies in its network. Eagleman et al. reported that oxygen vacancies are responsible for visible light emission in $La_2Hf_2O_7$.[49,50] In addition, we have found that electronic transition involving ionized oxygen vacancies are responsible for such luminescence properties from our earlier work on $Nd_2Zr_2O_7$ and $Gd_2Zr_2O_7$ pyrochlore.[5,27] The used excitation energy (~3.37 eV, 332 nm) is less than the band gap (3.42 eV) of GHO,[19,44] so direct transition from the valence band (VB) to the conduction band (CB) does not happen, and there exist certain localized defect states within the band gap of the GHO NPs. Such defects could arise during thermal treatment of the GHO NPs or may be present intrinsically in them.[51] The responsible oxygen vacancies for blue and red emission in the GHO-650 NPs are presented pictorially as a mechanism in Figure 3c. The blue emission could arise from the electronic transition of singly ionized oxygen vacancies to the VB, and the red emission from that of shallow oxygen defect vacancies to deep ones. The proposed different origins of these two emissions are consistent with the different excitation spectra obtained with λ_{em} = 445 and 720 nm at blue and red regions, respectively (Figure 3a).

2.5. PL Properties of the GHO:Eu^{3+}. *2.5.1. Excitation and Emission Spectroscopy.* Figure 4a shows the excitation spectra of the GHOE samples as a function of annealing temperature. These spectra consist of a very strong band peaking at ~263 nm, which is known as the charge transfer band (CTB) and attributed to electron transfer from a filled 2p orbital of O^{2-} ions to a vacant 4f orbital of the Eu^{3+} ion. The weak bands at 395 and 465 nm are due to $^7F_0 \rightarrow {}^5L_6$ and $^7F_0 \rightarrow {}^5D_2$ transitions of Eu^{3+} ions. The CTB as a La Porte-allowed transition has higher intensity than the forbidden f−f transitions. The excitation spectra monitored under various emission maxima (591, 630, 654, and 711 nm) are also shown in Figure S3a. Except for the marginal change in intensity, the spectra remain the same at different emission wavelengths. The emission spectra recorded with 263 nm excitation is shown in Figure 4b. For comparison,

DOI: 10.1021/acsomega.8b03458
ACS Omega 2019, 4, 2779−2791

emission spectra recorded under 263, 395, and 465 nm excitations are shown in Figure S3b. The intensity of the PL emission recorded with CTB excitation is much more intense than that with f−f excitation bands. The emission spectra for all three GHOE samples consist of five main peaks at 579, 591, 630, 654, and 711 nm corresponding to the $^5D_0 \rightarrow {}^7F_0$, $^5D_0 \rightarrow {}^7F_1$, $^5D_0 \rightarrow {}^7F_2$, $^5D_0 \rightarrow {}^7F_3$, and $^5D_0 \rightarrow {}^7F_4$ transitions, respectively. There are several interesting features of these spectra: appearance of $^5D_0 \rightarrow {}^7F_0$ transition that is allowed neither by magnetic dipole transition (MDT) nor by EDT, large splitting in the spectral peaks, high asymmetry ratio ($I^{5}_{D_0 \rightarrow {}^7F_2}/I^{5}_{D_0 \rightarrow {}^7F_1}$), and presence of relatively intense $^5D_0 \rightarrow {}^7F_4$ transition.

The presence of $^5D_0 \rightarrow {}^7F_0$ transition and large spectral splitting are signatures of the europium ion in highly disordered environment.[52] This is supported with the fact of relatively high emission intensity of $^5D_0 \rightarrow {}^7F_4$ transition due to a distorted chemical surrounding around the Eu^{3+} ions.[53] However, there are no changes of the spectral profile in terms of peak symmetry or width on changing the excitation wavelength.

Based on the emission spectra of the GHOE-650, GHOE-1100, and GHOE-1300 NPs (Figure 4b), three effects of annealing on the PL properties of the GHOE NPs were taken into consideration. These effects include (a) emission intensity, (b) spectral width of the $^5D_0 \rightarrow {}^7F_0$ emission lines, and (c) the ratio of integrated PL intensities between MDT ($^5D_0 \rightarrow {}^7F_1$) and hypersensitive EDTs ($^5D_0 \rightarrow {}^7F_2$), that is, the asymmetry ratio (I_{RO}).

First, the emission intensity of the $^5D_0 \rightarrow {}^7F_2$ EDT is much higher than that of the $^5D_0 \rightarrow {}^7F_1$ MDT for all three GHOE samples, suggesting that the Eu^{3+} ions are localized in low symmetry sites. Moreover, the PL emission intensity increases with increasing annealing temperature, which could be attributed to the different crystallite sizes of the GHOE NPs. The GHOE-650 NPs with the smallest size (~7 nm) have the highest surface to volume ratio, so are rich with surface defects. Such surface defects act as nonradiative pathways to decrease emission intensity. On the other hand, large-sized GHOE-1300 NPs have less surface defects with high emission intensity.

In all these three samples, the red emission due to $^5D_0 \rightarrow {}^7F_2$ transition is the most intense peak, and the color coordinates are very similar, so only one of the representative samples, that is, the GHOE-650 NPs, is shown with the International de l'Eclairage (CIE) diagram (Figure S3c).

2.5.2. Point Group Symmetry and Asymmetry Ratio of Eu^{3+} Ions in the GHOE NPs. Structural change of the GHO host can be corroborated with the change of Stark component numbers from the PL spectral pattern of Eu^{3+} ions, which is related to its point group symmetry.[54,55] The original point group symmetry of Gd^{3+}/Hf^{4+} sites in both OP and DF structures is D_{3d}.[16] Interestingly, the number of Stark components (as highlighted with black asterisks) of the EDT ($\Delta J = \pm 2$ and $\Delta J = \pm 4$) keeps increasing as the annealing temperature of the GHOE NPs increases as can be easily seen from Table S1. Such changes are clearly seen in the PL emission characteristics of $^5D_0 \rightarrow {}^7F_0$ (Figure 5a), $^5D_0 \rightarrow {}^7F_2$ (Figure 5b), and $^5D_0 \rightarrow {}^7F_4$ (Figure 5c) transitions as well. Accordingly, the point group symmetry of the GHO host reduces to C_{4v} for the GHOE-650 NPs because of lattice strain and distortion induced by the small particle size and charge mismatch of ions after Eu^{3+} doping. Furthermore, it changes to D_2 (for the GHOE-1100 NPs) and then to C_{2v} (for the GHOE-1300 NPs) because of the effects of annealing and structural change, as depicted schematically in Figure 5e.

The asymmetry ratio I_{RO} is also highly sensitive to structural change and useful to understand the local symmetry around the Eu^{3+} ions in the GHO host. As the GHO host goes from a highly DF structure to a highly OP structure, there is a progressive decrease of the asymmetry ratio of the Eu^{3+} ions (Figure 5d). The I_{RO} values of the GHOE-650, GHOE-1100, and GHOE-1300 NPs are 2.9, 2.0, and 1.6, respectively. This indicated that the local surrounding of Eu^{3+} ions is highly asymmetric in the GHOE-650 NPs with the DF structure, whereas the asymmetry becomes relatively low in the GHOE-1300 NPs with the OP structure. Therefore, the change of the I_{RO} values is in accordance with the structural difference of the GHOE NPs. Menushenkov et al. also found that the Debye Waller factor as the measure of root-mean-square deviation of the interatomic distance from the average value decreases with increasing annealing temperature for all Gd−O and Hf−O bonds of GHO by means of extended X-ray absorption fine structure measurements.[13] This confirms the increase of ordering of the crystalline structure with annealing temperature as reflected in the calculated I_{RO} values.

Neither MDT nor EDT allows $^5D_0 \rightarrow {}^7F_0$ transition of Eu^{3+} ions. However, it is still often observed from Eu^{3+}-doped inorganic phosphors because of the CF-induced *J*-mixing effect that lowers the symmetry.[56] According to the selection rule governing the EDT, this transition exists in low local symmetry situations of Eu^{3+} ions, including C_s, C_1, C_2, C_3, C_4, C_6, C_{2v}, C_{3v}, C_{4v}, and C_{6v}.[57] As shown in Figure 5a, the $^5D_0 \rightarrow {}^7F_0$ peak of the GHOE-650 NPs which are stabilized in the DF phase shows substantial intensity, and that of the GHOE-1100 and GHOE-1300 NPs is nearly absent because of the pyrochlore ordering.

Based on lifetime spectroscopy (Section 2.5.3), DFT-based cohesive energy calculations (Section 2.2), and local structure study (Section 2.3), Eu^{3+} ions can be stabilized at both Gd^{3+} and Hf^{4+} sites. Whatever the Stark component is considered in this work, it is based on composite emission spectra (Figure 3b) which have the contributions of Eu^{3+} ions at both Gd^{3+} and Hf^{4+} sites. To get individual emission spectra from these Eu@Gd and Eu@Hf sites, we need to carry out time-resolved emission spectroscopy (TRES) which can get individual spectra of Eu^{3+} ions at both Gd^{3+} and Hf^{4+} sites. We are trying to establish collaborations to use TRES as our future projects.

2.5.3. Excited State Lifetime and Quantum Yield. The $^5D_0$ emission decay profiles of all three GHOE samples at the $^5D_0 \rightarrow {}^7F_2$ transition display a biexponential behavior (Figure S4). Lifetime values were obtained by fitting with biexponential function

$$I(t) = I_0 + A_1 \exp(-t/\tau_1) + A_2 \exp(-t/\tau_2) \quad (1)$$

where τ_1 and τ_2 are actual lifetime values related to decay rates of corresponding exponential components, and A_1 and A_2 are biexponential fitting parameters. Based on the PL decay profiles corresponding to the $^5D_0$ excited state of Eu^{3+} ions in the GHOE NPs and the lifetime values obtained after biexponential fitting, the average lifetime values were calculated using the following equation

$$\tau_{av} = \frac{A_1\tau_1^{\,2} + A_2\tau_2^{\,2}}{A_1\tau_1 + A_2\tau_2} \quad (2)$$

The average and individual lifetime values were mentioned in Table 4. In the GHOE-650 NPs with the DF structure, Gd^{3+} ions exist in highly symmetric GdO_8 in the form of a cube, whereas Hf^{4+} ions exist in highly distorted octahedra. The short and long

DOI: 10.1021/acsomega.8b03458
ACS Omega 2019, 4, 2779−2791

Table 4. Luminescence Lifetime and Quantum Yield (QY) Values of the GHOE-650, GHOE-1100, and GHOE-1300 NPs

samples	τ_1 (ms)	τ_2 (ms)	τ_{avg} (ms)	χ^2	AQY (%)
GHOE-650	1.13	2.65	2.09	1.18	6.90
GHOE-1100	0.92	2.67	2.27	1.12	7.35
GHOE-1300	0.98	2.96	2.45	1.23	11.48

lifetimes can be explained by the presence of two different local sites of Eu^{3+} ions in the GHOE-650 NPs. The short one is attributed to Eu^{3+} ions occupying the distorted HfO_6 octahedra, whereas the long one is attributed to Eu^{3+} ions occupying the highly symmetric GdO_8 site. Eu^{3+} ions also exhibited biexponential decay in other pyrochlore hosts such as $La_2Hf_2O_7$, $Gd_2Zr_2O_7$, and $Nd_2Zr_2O_7$ wherein one of the lifetimes is attributed to A^{3+} site occupancy and other to B^{4+} site occupancy.[33,58−63] Normally, the short lifetime is attributed to asymmetric environment as f−f transition becomes relaxed, and the long lifetime is mostly attributed to symmetric environment as f−f transition is La Porte forbidden.[61,64−67] The biexponential behavior can also arise due to other reasons such as the presence of defects, energy transfer, and so forth. This phenomenon has been substantiated with theoretical calculations in the next section.

On the other hand, the GHOE-1100 and GHOE-1300 NPs have the prevailing OP structure where GdO_8 is highly distorted scalenohedra and HfO_6 exists in highly symmetrical octahedra. In this case, the longer lifetime is attributed to Eu^{3+} ions sitting at HfO_6 sites, whereas the shorter one is due to Eu^{3+} ions localized at the distorted GdO_8 site.

The average lifetime values of the GHOE-650, GHOE-1100, and GHOE-1300 NPs were 2.09, 2.27, and 2.45 ms, respectively. The increasing average lifetime values is partially due to the decreasing distortion of Eu^{3+} ions in the GHO NPs with increasing annealing temperature. In addition, the surface defect density is the least for the GHOE-1300 NPs, so they have the lowest relaxation probability through nonradiative transitions, and hence the highest lifetime value.

Furthermore, the lower the nonradiative transition probability, the higher the quantum efficiency. With the highest absolute quantum yield (AQY) reported (Table 4), it is suggested that the GHOE-1300 NPs are the most suitable sample for optical emitter and fluoroimmunoassay applications wherein a high lifetime is needed. The lowest lifetime value from the GHOE-650 NPs is also reflected in the minimal AQY among all three samples.

Judd−Ofelt analysis was carried out for the GHOE-650, GHOE-1100, and GHOE-1300 NPs with their radiative transition rate (A_R), nonradiative transition rate (A_{NR}), internal quantum efficiency (IQY), Judd−Ofelt parameters (short and long range), and branching ratio values (Table 5). As discussed earlier, the symmetry increases with increasing annealing temperature for the GHOE NPs, especially for the GHOE-1300 NPs with a highly OP structure. This trend in short-range and long-range Judd−Ofelt parameters was justified with $\Omega_2 > \Omega_4$ because the Ω_2 and Ω_4 values are highly sensitive to the local structure around the Eu^{3+} ions. It is also reflected with the highest and the lowest branching ratios of β_1 and β_2 from the GHOE-1300 NPs, respectively, indicating the most contribution of MDT in their PL emission process. On the contrary, the β_2 value of the GHOE-650 NPs is the highest, and the β_1 value is the lowest among the three samples. The trend of the IQY values closely matches to that of the AQY values, consistent with the A_R and A_{NR} values.

2.5.4. RL Spectroscopy. RL spectra of the GHOE NPs (Figure 6a) consist of typical Eu^{3+} ion peaks from the forbidden EDT 4f → 4f ($^5D_0 \rightarrow {}^7F_J$, $J = 0-4$) transitions in the visible range of 550−750 nm. Materials that can efficiently absorb and convert high-energy radiation such as X-ray or γ ray into visible light can display wide array of applications in medical imaging, radiation detection, and scientific instrumentation.[68] In this context, our GHOE samples display unique ability to convert highly energetic X-ray radiation into visible light based on the RL spectrum.

For the GHOE-650 NPs, the EDT peak around 612 nm is more intense than the MDT peak at 592 nm with intense red emission because of the highly DF structure. After annealing at 1100 and 1300 °C, there is reversal of the EDT and MDT peak pattern. Now, the MDT peak overpowers the EDT one indicating the stabilization of the Eu^{3+} ion in highly OPP, consistent with previous results. Hence, the emission color changes from red to orange (Figure 6c), showing the RL tunability. Furthermore, the more intense MDT peak of the GHOE-1300 NPs suggests that most of the Eu^{3+} ions are located at sites with inversion symmetry, consistent with the asymmetry ratio values (Figure 6b). Figure 6d shows the RL emission spectra because of the presence of some divalent europium ion resulted from the reduction of some of the Eu^{3+} ions on irradiation with highly energetic X-ray. The peak around 545 nm is ascribed to the electric dipole-allowed transition $4f^6 5d \rightarrow {}^8S_{7/2}$ ($4f^7$) of the Eu^{2+} ions. Interestingly, the GHOE-650 NPs have the highest fraction of the divalent europium ion, whereas the GHOE-1300 NPs have the least. This phenomenon is possibly (i) due to the smallest particle size of the GHOE-650 NPs, and hence the largest numbers of exposed Eu^{3+} ions on the surface or the subsurface are subjected to the reduction reaction by X-ray irradiation or (ii) the DF versus OP structure of GHOE-650 versus GHOE-1300 NPs.

The emission spectra under UV photon and X-ray are different because the luminescence mechanisms involved in these two cases are distinct. Specifically, under X-ray excitation, e^-−h^+ pairs (excitons) are generated, and the Eu^{3+} 4f−4f bands and hosts are excited together.[33,58,59,69] In this situation, e^- migrates to the Eu^{3+} centers before luminescence. Under UV excitation, only the Eu^{3+} (4f−4f) bands are excited, but not the host. Moreover, the conversion of X-ray excitation into visible light usually proceeds in four different steps. In the first step, GHOE absorbs an X-ray through the photoelectric effect and leads to creation of electron and holes. In the second step, these electrons and holes relax to generate large number of secondary

Table 5. Judd−Ofelt Analysis of the GHOE NPs

samples	A_R (s^{-1})	A_{NR} (s^{-1})	IQY (%)	Ω_2 ($\times 10^{-21}$)	Ω_4 ($\times 10^{-21}$)	β_1 (%)	β_2 (%)	β_3 (%)
GHOE-650	236	198	54.3	4.97	3.12	17.8	59.7	18.8
GHOE-1100	265	184	59.6	5.26	3.86	18.9	58.1	21.9
GHOE-1300	281	172	62.1	4.22	3.21	21.1	56.8	21.6

DOI: 10.1021/acsomega.8b03458
ACS Omega 2019, 4, 2779−2791

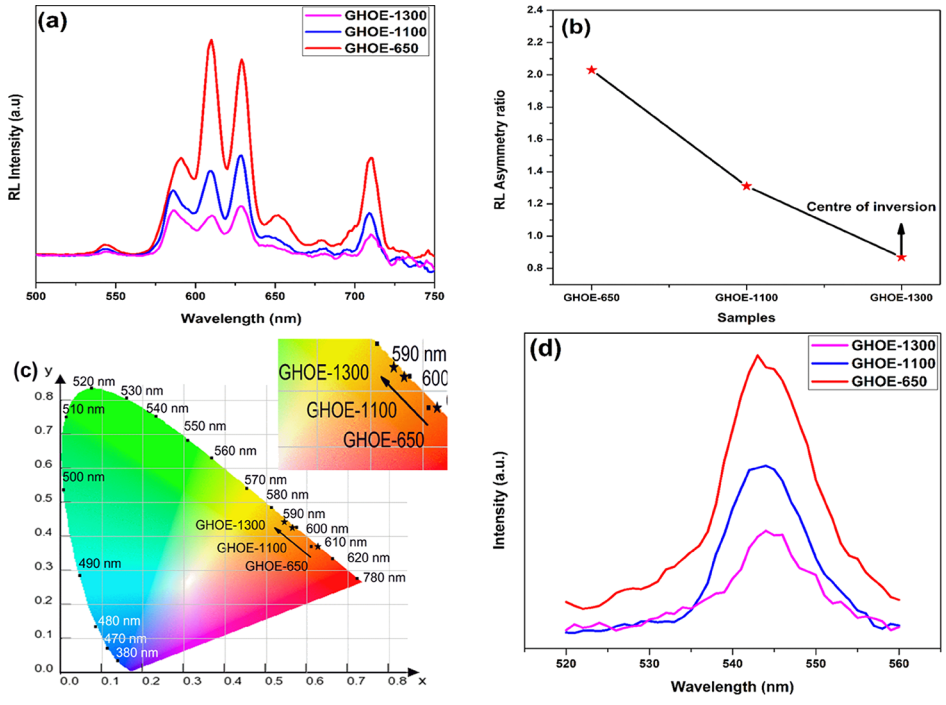

Figure 6. (a) RL spectra, (b) variation of the RL asymmetry ratio, (c) chromaticity coordinate diagram, and (d) RL emission due to the Eu^{2+} ion (because of the reduction of the Eu^{3+} ions by X-ray irradiation) of the GHOE NPs.

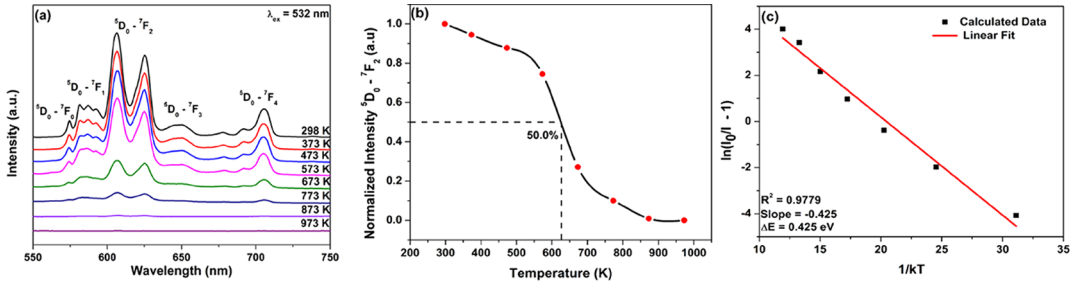

Figure 7. (a) Emission spectra at temperatures ranging from 298 to 973 K, (b) corresponding temperature dependence of the PL emission intensity of the $^5D_0 \rightarrow {}^7F_2$ transition, and (c) plot of $\ln(I_0/I - 1)$ vs $1/kT$ of the GHOE-650 NPs.

electrons, holes, photons, and plasmons. Such relaxation also induces several other electronic excitations. These secondary electrons and holes lose their energy via electron−phonon interaction to give electron−hole pairs with near band gap energy. The third stage involves the transport of the electron−hole pairs (excitons) through the host material to a luminescent center (trap) and the excitation of the luminescent center. The final stage concerns the resulting luminescence. Materials which have a high light output and a short lifetime under photo-excitation may have a very low light output and/or a long lifetime under X-ray excitation. This is due to the energy losses and delays in the energy migration processes, which are absent in PL where the luminescent centers are directly and intentionally excited.

2.5.5. Thermal Quenching Behavior of GHOE NPs. Thermal stability of phosphors is a very important property for their applications toward solid-state lighting and high-power light-emitting diodes. Therefore, we have carried out emission spectroscopy of the GHOE-650 NPs at various temperatures using in situ PL measurements. Figure 7a shows emission spectra of the GHOE NPs measured from room temperature to 973 K. The spectral features do not change with the increase of temperature. At 298 K, the GHOE-650 NPs exhibit intense red emission because of hypersensitive electric dipole $^5D_0 \rightarrow {}^7F_2$ transition. However, as temperature increases, there is monotonic reduction in emission intensity (Figure 7b). Such thermal quenching is attributed to a crossover mechanism wherein europium ions are thermally activated through the crossing point between the ground and the excited states.[70] The quenching temperature, $T_{0.5}$, at which the emission intensity drops to 50% of that at room temperature, is about 625 K, indicating an extremely high thermal stability of the GHOE NPs. The thermal population of the charge transfer state ($^5D \rightarrow CT \rightarrow {}^7F$) or the excited state ($^5D \rightarrow {}^7F$) increases the chances of nonradiative relaxation.[71]

In addition, the thermal quenching activation energy of the GHOE NPs was extrapolated from the slope of Figure 7c denoted from the following Arrhenius equation[59]

$$\ln\left(\frac{I_o}{I} - 1\right) = \ln A - \frac{\Delta E}{kT} + C \tag{3}$$

where I_o is initial emission intensity, and I is the emission intensity at a given temperature T. For a given constant A and a fixed value of Boltzmann constant k, ΔE denotes the activation

DOI: 10.1021/acsomega.8b03458
ACS Omega 2019, 4, 2779−2791

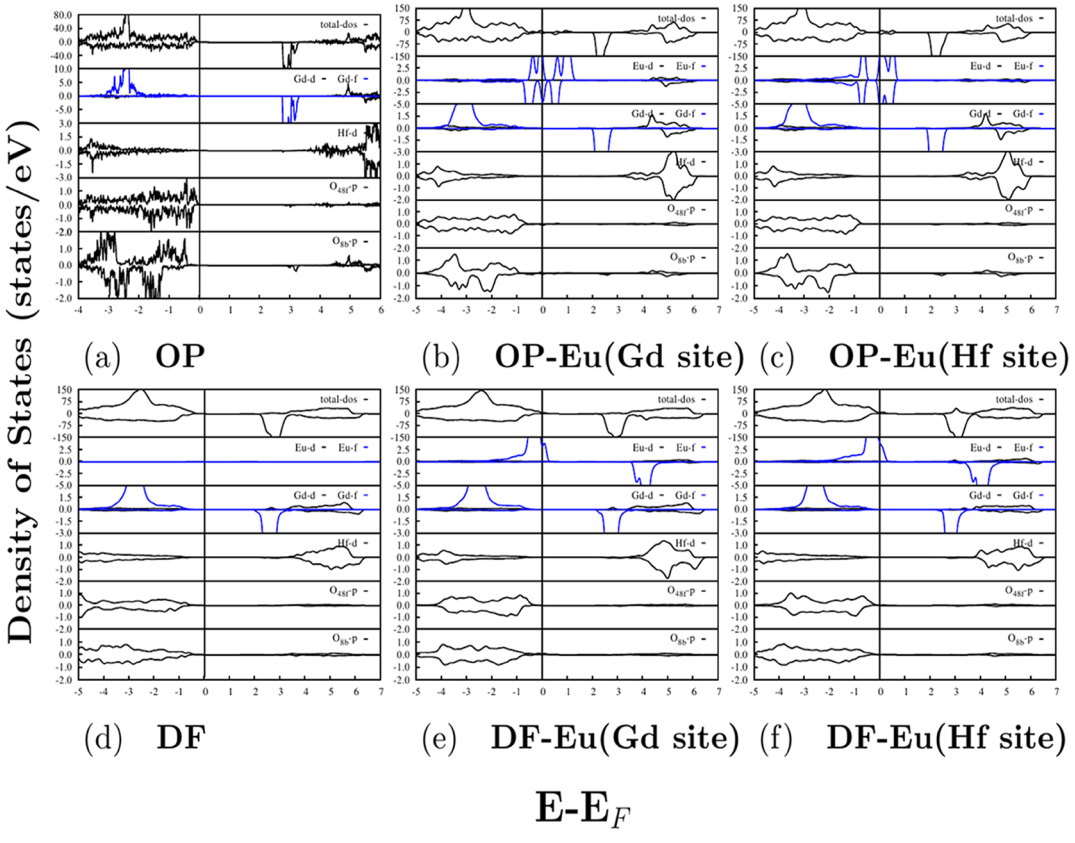

Figure 8. DFT-GGA calculated total and partial DOSs of the (a) OP structure, (b) Eu doped at the Gd site in the OP structure, (c) Eu doped at the Hf site in the OP structure, (d) DF structure, (e) Eu doped at the Gd site in the DF structure, and (f) Eu doped at the Hf site in the DF structure.

energy involved in thermal quenching process. The relationship of $\ln(I_0/I - 1)$ and $1/kT$ displayed linear behavior (Figure 7c). The activation energy calculated from this plot is equal to 0.425 eV for the thermal quenching. In our earlier work on $La_2Hf_2O_7:Eu^{3+}$ NPs with an ideal pyrochlore structure, the activation energy value was found to be 0.410 eV which is slightly lower than the defect fluorite GHOE-650 NPs.[59]

2.6. Efficiency of Host to Dopant Energy Transfer by DFT Calculations. Based on the DFT-GGA-calculated total and partial DOSs, VBs from −4 to 0 eV of the OP structure have a main contribution from the O 2p states and a small contribution from the Gd 5d states (Figure 8a). The energy range is scaled with respect to Fermi energy (E_F), and the E_F is set at 0 eV. The upper and lower panels show DOS contributions from spin-up and spin-down components, respectively. The peak around −2.5 eV corresponds to Gd f states in the spin-up component. The lower part of the VB is dominantly contributed by the Hf d states in both spin components. The O 2p states are contributing throughout the VB. In the CB, a peak around 5.0 eV represents Gd d states with a small admixture of the O p states. At the edge of the CB, Gd f states contribute in the spin-down component. As a result, the electronic band gaps in spin-up and spin-down components are 3.45 and 2.56 eV, respectively. Figure 8b,c shows the DFT-GGA-calculated DOSs of GHO with Eu doped at Gd and Hf sites, respectively. The overall DOSs have resemblance with ideal GHO. Eu f states contribute strongly at the VB edge in both spin-up and spin-down components. As a result, impurity states are generated at the VB edge around the E_F level.

For the DF structure, the DOS features (Figure 8d−f) are similar to those of the OP structure. However, less number of peaks presented in the DOSs of the DF structure signifies positional disordering. In the DOSs of Eu-doped DF, Eu f states contribute solely on the edges of the VB and the CB in spin-up and spin-down components. The electrons present at the VB edges participate in the photoexcitation. High contribution of Eu f states at the VB edges makes optical energy transfer of the GHO host to Eu^{3+} dopants favorable.

3. CONCLUSIONS

In this work, we have investigated the effect of structural changes of GHO NPs on their PL and RL using europium ions as a spectroscopic probe. GHO and GHO:Eu^{3+} (GHOE) NPs were synthesized by a MSS method at 650 °C and subjected to annealing at 1100 and 1300 °C with structural evolution. Raman spectroscopy confirms the stabilization of the GHOE-650 NPs with DFP, whereas the GHOE-1300 NPs with a perfectly OP structure. The structure evolution from the fluorite to pyrochlore phase renders a decreased asymmetry ratio of the Eu^{3+} dopant. Moreover, annealing of the GHOE NPs increases the luminescence emission intensity, quantum efficiency, excited state lifetime, and Stark components, and change the Eu local symmetry from C_{4v} (GHOE-650) to D_2 (GHOE-1100) to C_{2v} (GHOE-1300). The effect of disorder−order transition is also evident from RL wherein the emission color changes from red to orange. High thermal stability is an added advantage of this phosphor for application in solid-state lighting. Our DFT results are corroborating with our experimental findings. Moreover, DFT DOSs analysis shows favorable localization of Eu f states in the VB of GHO, which makes host to dopant optical energy transfer possible.

DOI: 10.1021/acsomega.8b03458
ACS Omega 2019, 4, 2779−2791

4. EXPERIMENTAL: SYNTHESIS AND CHARACTERIZATION

$Gd_2Hf_2O_7$ (GHO) and Eu^{3+}-doped GHO (GHOE) NPs were synthesized using MSS at 650 °C (GHO-650 and GHOE-650), similar to our earlier work for $La_2Hf_2O_7$ NPs.[2,4] However, by doping europium ions into the GHO host, Gd^{3+} ions are replaced based on closeness in terms of ionic radius and ionic charge. The GHOE-650 sample was further annealed at 1100 and 1300 °C in air for 6 h, and the products are noted as GHOE-1100 and GHOE-1300, respectively. The details of synthesis, characterization, theoretical methodology, Judd−Ofelt analysis, and QY measurements are included in the Supporting Information as S1−S5, respectively.

■ ASSOCIATED CONTENT

Supporting Information

The Supporting Information is available free of charge on the ACS Publications website at DOI: 10.1021/acsomega.8b03458.

Details of synthesis, characterization, and theoretical methodology (PDF)

■ AUTHOR INFORMATION

Corresponding Author

*E-mail: yuanbing.mao@utrgv.edu. Phone: +1-956-665-2986 (Y.M.).

ORCID

Santosh K. Gupta: 0000-0002-1178-0159

Yuanbing Mao: 0000-0003-2665-6676

Notes

The authors declare no competing financial interest.

■ ACKNOWLEDGMENTS

The authors acknowledge financial support by the National Science Foundation under CHE (award #1710160) and DMR (grant #1523577) and the USDA National Institute of Food and Agriculture (award #2015-38422-24059). The Department of Chemistry at the University of Texas Rio Grande Valley is grateful for the generous support provided by a Departmental Grant from the Robert A. Welch Foundation (grant no. BX-0048). The in situ emission spectra were conducted at the Center for Nanophase Materials Science, which is a U.S. Department of Energy, Office of Science User Facility, and the authors thank Dr. A. Puretzky for technical assistance. S.K.G. thanks the United States−India Education Foundation (USIEF) and the Institute of International Education (IIE) for his Fulbright Nehru Postdoctoral Fellowship (award# 2268/FNPDR/2017).

■ REFERENCES

(1) Zhang, W.; Tao, Y.; Li, C. Sol-gel synthesize and characterization of $\chi Gd_2Ti_2O_7/SiO_2$ photocatalyst for ofloxacin decomposition. *Mater. Res. Bull.* **2018**, *105*, 55−62.

(2) Zuniga, J. P.; Gupta, S. K.; Pokhrel, M.; Mao, Y. Exploring the optical properties of $La_2Hf_2O_7:Pr^{3+}$ nanoparticles under UV and X-ray excitation for potential lighting and scintillating applications. *New J. Chem.* **2018**, *42*, 9381−9392.

(3) Gupta, S. K.; Reghukumar, C.; Pathak, N.; Sudarshan, K.; Tyagi, D.; Mohapatra, M.; Pujari, P. K.; Kadam, R. M. Speciation of uranium and doping induced defects in $Gd_{1.98}U_{0.02}Zr_2O_7$: Photoluminescence, X-ray photoelectron and positron annihilation lifetime spectroscopy. *Chem. Phys. Lett.* **2017**, *669*, 245−250.

(4) Wahid, K.; Pokhrel, M.; Mao, Y. Structural, photoluminescence and radioluminescence properties of Eu^{3+} doped $La_2Hf_2O_7$ nanoparticles. *J. Solid State Chem.* **2017**, *245*, 89−97.

(5) Gupta, S. K.; Sudarshan, K.; Ghosh, P. S.; Srivastava, A. P.; Bevara, S.; Pujari, P. K.; Kadam, R. M. Role of various defects in the photoluminescence characteristics of nanocrystalline $Nd_2Zr_2O_7$: an investigation through spectroscopic and DFT calculations. *J. Mater. Chem. C* **2016**, *4*, 4988−5000.

(6) Sibille, R.; Gauthier, N.; Yan, H.; Ciomaga Hatnean, M.; Ollivier, J.; Winn, B.; Filges, U.; Balakrishnan, G.; Kenzelmann, M.; Shannon, N.; Fennell, T. Experimental signatures of emergent quantum electrodynamics in $Pr_2Hf_2O_7$. *Nat. Phys.* **2018**, *14*, 711−715.

(7) Yang, J.; Han, Y.; Shahid, M.; Pan, W.; Zhao, M.; Wu, W.; Wan, C. A promising material for thermal barrier coating: Pyrochlore-related compound Sm_2FeTaO_7. *Scr. Mater.* **2018**, *149*, 49−52.

(8) Bayart, A.; Szczepanski, F.; Blach, J.-F.; Rousseau, J.; Katelnikovas, A.; Saitzek, S. Upconversion luminescence properties and thermal quenching mechanisms in the layered perovskite $La_{1.9}Er_{0.1}Ti_2O_7$ towards an application as optical temperature sensor. *J. Alloys Compd.* **2018**, *744*, 516−527.

(9) Zhang, S.; Zhang, H. B.; Zhao, F. A.; Jiang, M.; Xiao, H. Y.; Liu, Z. J.; Zu, X. T. Impact of isovalent and aliovalent substitution on the mechanical and thermal properties of $Gd_2Zr_2O_7$. *Sci. Rep.* **2017**, *7*, 6399.

(10) Rittman, D. R.; Turner, K. M.; Park, S.; Fuentes, A. F.; Park, C.; Ewing, R. C.; Mao, W. L. Strain engineered pyrochlore at high pressure. *Sci. Rep.* **2017**, *7*, 2236.

(11) Paul, B.; Singh, K.; Jaroń, T.; Roy, A.; Chowdhury, A. Structural properties and the fluorite−pyrochlore phase transition in $La_2Zr_2O_7$: The role of oxygen to induce local disordered states. *J. Alloys Compd.* **2016**, *686*, 130−136.

(12) Park, S.; Tracy, C. L.; Zhang, F.; Park, C.; Trautmann, C.; Tkachev, S. N.; Lang, M.; Mao, W. L.; Ewing, R. C. Radiation-induced disorder in compressed lanthanide zirconates. *Phys. Chem. Chem. Phys.* **2018**, *20*, 6187−6197.

(13) Menushenkov, A. P.; Popov, V. V.; Zubavichus, Y. V.; Yaroslavtsev, A. A. Local peculiarities of the nanocrystalline structure of ternary oxides $Ln_2Hf_2O_7$ (Ln= Gd, Tb, Dy). *J. Struct. Chem.* **2017**, *57*, 1450−1458.

(14) Durand, A. M.; Klavins, P.; Corruccini, L. R. Heat capacity of the frustrated magnetic pyrochlores $Gd_2Zr_2O_7$ and $Gd_2Hf_2O_7$. *J. Phys.: Condens. Matter* **2008**, *20*, 235208.

(15) Ali Biswas, A.; Jana, Y. Study on the low-temperature properties of pyrochlores $Gd_2Hf_2O_7$ and $Gd_2Zr_2O_7$, using crystal-field theory. *AIP Conference Proceedings*; AIP, 2011; pp 1121−1122.

(16) Kumar, S.; Gupta, H. C. First principles study of dielectric and vibrational properties of pyrochlore hafnates. *Solid State Sci.* **2012**, *14*, 1405−1411.

(17) Cepeda-Sánchez, N. M.; Fuentes, A. F.; López-Cota, F. A.; Rodríguez-Reyes, M.; Díaz-Guillén, J. A. Mechanochemical synthesis and electrical properties of $Gd_2Hf_{2-x}Zr_xO_7$ solid electrolytes for their use in SOFC's. *J. Appl. Electrochem.* **2015**, *45*, 1231−1237.

(18) Sevastyanov, V. G.; Simonenko, E. P.; Simonenko, N. P.; Stolyarova, V. L.; Lopatin, S. I.; Kuznetsov, N. T. Synthesis, vaporization and thermodynamic properties of superfine $Nd_2Hf_2O_7$ and $Gd_2Hf_2O_7$. *Eur. J. Inorg. Chem.* **2013**, 4636−4644.

(19) Chen, C. F.; Brennecka, G. L.; Synowicki, R. A.; Tegtmeier, E. L.; Brand, M. J.; Montalvo, J. D.; Ivy, J.; Cherepy, N. J.; Seeley, Z.; Payne, S. A. Transparent polycrystalline $Gd_2Hf_2O_7$ ceramics. *J. Am. Ceram. Soc.* **2018**, *101*, 3797−3807.

(20) Chen, C.-F.; Brennecka, G. L.; Synowicki, R. A.; Tegtmeier, E. L.; Brand, M. J.; Montalvo, J. D.; Ivy, J.; Cherepy, N. J.; Seeley, Z.; Payne, S. A. Transparent polycrystalline $Gd_2Hf_2O_7$ ceramics. *J. Am. Ceram. Soc.* **2018**, *101*, 3797.

(21) Shannon, R. D. Revised effective ionic radii and systematic studies of interatomic distances in halides and chalcogenides. *Acta Crystallogr., Sect. A: Cryst. Phys., Diffr., Theor. Gen. Crystallogr.* **1976**, *32*, 751−767.

(22) Zhang, X.; Hayakawa, T.; Nogami, M.; Ishikawa, Y. Selective synthesis and luminescence properties of nanocrystalline $GdF_3:Eu^{3+}$

DOI: 10.1021/acsomega.8b03458
ACS Omega 2019, 4, 2779−2791

with hexagonal and orthorhombic structures. *J. Nanomater.* **2010**, *2010*, 1.
(23) Tian, Y.; Hua, R.; Chen, B.; Yu, N.; Zhang, W.; Na, L. Lanthanide dopant-induced phase transition and luminescent enhancement of EuF_3 nanocrystals. *CrystEngComm* **2012**, *14*, 8110−8116.
(24) Papan, J.; Jovanović, D. J.; Vuković, K.; Smits, K.; Đorđević, V.; Dramićanin, M. Europium (III)-doped $A_2Hf_2O_7$ (A= Y, Gd, Lu) nanoparticles: Influence of annealing temperature, europium (III) concentration and host cation on the luminescent properties. *Opt. Mater.* **2016**, *61*, 68−76.
(25) Pokhrel, M.; Wahid, K.; Mao, Y. Systematic studies on $RE_2Hf_2O_7$:5%Eu^{3+} (RE= Y, La, Pr, Gd, Er, and Lu) nanoparticles: effects of the A-site RE^{3+} cation and calcination on structure and photoluminescence. *J. Phys. Chem. C* **2016**, *120*, 14828−14839.
(26) Garbout, A.; Kallel- Kchaou, N.; Férid, M. Relationship between the structural characteristics and photoluminescent properties of $LnEuTi_2O_7$ (Ln=Gd and Y) pyrochlores. *J. Lumin.* **2016**, *169*, 359−366.
(27) Gupta, S. K.; Ghosh, P. S.; Reghukumar, C.; Pathak, N.; Kadam, R. M. Experimental and theoretical approach to account for green luminescence from $Gd_2Zr_2O_7$ pyrochlore: exploring the site occupancy and origin of host-dopant energy transfer in $Gd_2Zr_2O_7$:Eu^{3+}. *RSC Adv.* **2016**, *6*, 44908−44920.
(28) Ćulubrk, S.; Antić, Ž.; Lojpur, V.; Marinović-Cincović, M.; Dramićanin, M. D. Sol-Gel derived Eu^{3+}-doped $Gd_2Ti_2O_7$ pyrochlore nanopowders. *J. Nanomater.* **2015**, *2015*, 514173.
(29) Ćulubrk, S.; Antić, Ž.; Marinović-Cincović, M.; Ahrenkiel, P. S.; Dramićanin, M. D. Synthesis and luminescent properties of rare earth (Sm^{3+} and Eu^{3+}) Doped $Gd_2Ti_2O_7$ pyrochlore nanopowders. *Opt. Mater.* **2014**, *37*, 598−606.
(30) Zhang, Y.; Jia, C.; Su, Z.; Zhang, W. The enhanced and color-tunable photoluminescence of Eu^{3+}/V^{5+} co-doped $Gd_2Ti_2O_7$ nanocrystals. *J. Alloys Compd.* **2009**, *479*, 381−384.
(31) Liao, J.; Nie, L.; Wang, Q.; Liu, S.; Fu, J.; Wen, H.-R. Microwave hydrothermal method and photoluminescence properties of $Gd_2Sn_2O_7$:Eu^{3+} reddish orange phosphors. *J. Lumin.* **2017**, *183*, 377−382.
(32) Gupta, S. K.; Sudarshan, K.; Ghosh, P. S.; Sanyal, K.; Srivastava, A. P.; Arya, A.; Pujari, P. K.; Kadam, R. M. Luminescence of undoped and Eu^{3+} doped nanocrystalline $SrWO_4$ scheelite: time resolved fluorescence complimented by DFT and positron annihilation spectroscopic studies. *RSC Adv.* **2016**, *6*, 3792−3805.
(33) Gupta, S. K.; Zuniga, J. P.; Abdou, M.; Mao, Y. Thermal annealing effects on $La_2Hf_2O_7$:Eu^{3+} nanoparticles: A curious case study of structural evolution and site-specific photo- and radio-luminescence. *Inorg. Chem. Front.* **2018**, *5*, 2508−2521.
(34) Gupta, S. K.; Sudarshan, K.; Ghosh, P. S.; Srivastava, A. P.; Bevara, S.; Pujari, P. K.; Kadam, R. M. Role of various defects in the photoluminescence characteristics of nanocrystalline $Nd_2Zr_2O_7$: an investigation through spectroscopic and DFT calculations. *J. Mater. Chem. C* **2016**, *4*, 4988−5000.
(35) Gupta, S. K.; Rajeshwari, B.; Achary, S. N.; Patwe, S. J.; Tyagi, A. K.; Natarajan, V.; Kadam, R. M. Europium Luminescence as a Structural Probe: Structure-Dependent Changes in Eu^{3+}-Substituted $Th(C_2O_4)_2{\cdot}xH_2O$ (x= 6, 2, and 0). *Eur. J. Inorg. Chem.* **2015**, 4429−4436.
(36) Popov, V. V.; Petrunin, V. F.; Korovin, S. A.; Menushenkov, A. P.; Kashurnikova, O. V.; Chernikov, R. V.; Yaroslavtsev, A. A.; Zubavichus, Y. V. Formation of nanocrystalline structures in the Ln_2O_3-MO_2 systems (Ln = Gd, Dy; M = Zr, Hf). *Russ. J. Inorg. Chem.* **2011**, *56*, 1538.
(37) Popov, V. V.; Zubavichus, Y. V.; Petrunin, V. F.; Menushenkov, A. P.; Kashurnikova, O. V.; Korovin, S. A.; Chernikov, R. V.; Yaroslavtsev, A. A. A study of the formation of $Ln_{2+x}Me_{2-x}O_{7-x/2}$ (Ln = Gd, Dy; Me = Zr, Hf) nanocrystals. *Glass Phys. Chem.* **2011**, *37*, 512.
(38) Popov, V. V.; Menushenkov, A. P.; Zubavichus, Y. V.; Yaroslavtsev, A. A.; Leshchev, D. S.; Kulik, E. S.; Bednarcik, J.; Petrunin, V. F.; Korovin, S. A.; Chernikov, R. V. Characteristic features of the nanocrystalline structure formation in $Ln_2Hf_2O_7$ (Ln = Gd, Dy) compounds. *Russ. J. Inorg. Chem.* **2013**, *58*, 1400−1407.
(39) Sayed, F. N.; Grover, V.; Bhattacharyya, K.; Jain, D.; Arya, A.; Pillai, C. G. S.; Tyagi, A. K. $Sm_{2-x}Dy_xZr_2O_7$ Pyrochlores: Probing Order− Disorder Dynamics and Multifunctionality. *Inorg. Chem.* **2011**, *50*, 2354−2365.
(40) Turner, K. M.; Rittman, D. R.; Heymach, R. A.; Tracy, C. L.; Turner, M. L.; Fuentes, A. F.; Mao, W. L.; Ewing, R. C. Pressure-induced structural modifications of rare-earth hafnate pyrochlore. *J. Phys.: Condens. Matter* **2017**, *29*, 255401.
(41) Subramanian, M. A.; Aravamudan, G.; Subba Rao, G. V. Oxide pyrochlores - A review. *Prog. Solid State Chem.* **1983**, *15*, 55−143.
(42) Garg, N.; Pandey, K.; Murli, C.; Shanavas, K.; Mandal, B. P.; Tyagi, A.; Sharma, S. M. Decomposition of lanthanum hafnate at high pressures. *Phys. Rev. B: Condens. Matter Mater. Phys.* **2008**, *77*, 214105.
(43) Ushakov, S. V.; Navrotsky, A.; Tangeman, T. A.; Helean, K. B. Energetics of Defect Fluorite and Pyrochlore Phases in Lanthanum and Gadolinium Hafnates. *J. Am. Ceram. Soc.* **2007**, *90*, 1171−1176.
(44) Li, N.; Xiao, H. Y.; Zu, X. T.; Wang, L. M.; Ewing, R. C.; Lian, J.; Gao, F. First-principles study of electronic properties of $La_2Hf_2O_7$ and $Gd_2Hf_2O_7$. *J. Appl. Phys.* **2007**, *102*, 063704.
(45) Jiang, C.; Stanek, C. R.; Sickafus, K. E.; Uberuaga, B. P. First-principles prediction of disordering tendencies in pyrochlore oxides. *Phys. Rev. B: Condens. Matter Mater. Phys.* **2009**, *79*, 104203.
(46) Li, Y.; Kowalski, P. M.; Beridze, G.; Birnie, A. R.; Finkeldei, S.; Bosbach, D. Defect formation energies in $A_2B_2O_7$ pyrochlores. *Scr. Mater.* **2015**, *107*, 18−21.
(47) Gupta, S. K.; Ghosh, P. S.; Pathak, N.; Arya, A.; Natarajan, V. Understanding the local environment of Sm^{3+} in doped $SrZrO_3$ and energy transfer mechanism using time-resolved luminescence: a combined theoretical and experimental approach. *RSC Adv.* **2014**, *4*, 29202−29215.
(48) Nakamura, K.; Mori, M.; Itoh, T.; Ohnuma, T. Theoretical and experimental investigation of defect formation / migration in Gd2Ti2O7: General rule of oxide-ion migration in A2B2O7 pyrochlore. *AIP Adv.* **2016**, *6*, 115003.
(49) Eagleman, Y.; Weber, M.; Chaudhry, A.; Derenzo, S. Luminescence study of cerium-doped $La_2Hf_2O_7$: Effects due to trivalent and tetravalent cerium and oxygen vacancies. *J. Lumin.* **2012**, *132*, 2889−2896.
(50) Eagleman, Y.; Weber, M.; Derenzo, S. Luminescence study of oxygen vacancies in lanthanum hafnium oxide, $La_2Hf_2O_7$. *J. Lumin.* **2013**, *137*, 93−97.
(51) Zhang, B.; Dewasurendra, S.; Zhang, F. X. Blue and red up-conversion light emission in TM-doped $A_2B_2O_7$ oxides. *Mater. Lett.* **2016**, *170*, 53−57.
(52) Gupta, S. K.; Mohapatra, M.; Kaity, S.; Natarajan, V.; Godbole, S. V. Structure and site selective luminescence of sol−gel derived Eu: Sr_2SiO_4. *J. Lumin.* **2012**, *132*, 1329−1338.
(53) Ferreira, R. A. S.; Nobre, S. S.; Granadeiro, C. M.; Nogueira, H. I. S.; Carlos, L. D.; Malta, O. L. A theoretical interpretation of the abnormal $^5D_0 \rightarrow {}^7F_4$ intensity based on the Eu^{3+} local coordination in the $Na_9[EuW_{10}O_{36}]{\cdot}14H_2O$ polyoxometalate. *J. Lumin.* **2006**, *121*, 561−567.
(54) Ju, Q.; Liu, Y.; Li, R.; Liu, L.; Luo, W.; Chen, X. Optical Spectroscopy of Eu3+-Doped BaFCl Nanocrystals. *J. Phys. Chem. C* **2009**, *113*, 2309−2315.
(55) Binnemans, K. Interpretation of europium(III) spectra. *Coord. Chem. Rev.* **2015**, *295*, 1−45.
(56) Chen, X. Y.; Zhao, W.; Cook, R. E.; Liu, G. K. Anomalous luminescence dynamics of Eu^{3+} in BaFCl microcrystals. *Phys. Rev. B: Condens. Matter Mater. Phys.* **2004**, *70*, 205122.
(57) Gupta, S. K.; Bhide, M. K.; Godbole, S. V.; Natarajan, V. Probing Site Symmetry Around Eu^{3+} in Nanocrystalline ThO_2 Using Time Resolved Emission Spectroscopy. *J. Am. Ceram. Soc.* **2014**, *97*, 3694−3701.
(58) Zuniga, J. P.; Gupta, S. K.; Abdou, M.; Mao, Y. Effect of Molten Salt Synthesis Processing Duration on the Photo- and Radio-luminescence of UV-, Visible-, and X-ray-Excitable$Gd_2Hf_2O_7$:Eu^{3+} Nanoparticles. *ACS Omega* **2018**, *3*, 7757−7770.

DOI: 10.1021/acsomega.8b03458
ACS Omega 2019, 4, 2779−2791

(59) Gupta, S. K.; Zuniga, J. P.; Ghosh, P. S.; Abdou, M.; Mao, Y. Correlating Structure and Luminescence Properties of Undoped and $La_2Hf_2O_7$:Eu^{3+}NPs Prepared with Different Coprecipitating pH Values through experimental and theoretical studies. *Inorg. Chem.* **2018**, *57*, 11815−11830.
(60) Pokhrel, M.; Wahid, K.; Mao, Y. Systematic studies on $RE_2Hf_2O_7$:5% Eu^{3+} (RE= Y, La, Pr, Gd, Er, and Lu) nanoparticles: effects of the A-site RE^{3+} cation and calcination on structure and photoluminescence. *J. Phys. Chem. C* **2016**, *120*, 14828−14839.
(61) Gupta, S. K.; Reghukumar, C.; Kadam, R. M. Eu^{3+} local site analysis and emission characteristics of novel $Nd_2Zr_2O_7$:Eu phosphor: insight into the effect of europium concentration on its photoluminescence properties. *RSC Adv.* **2016**, *6*, 53614−53624.
(62) Gupta, S. K.; Ghosh, P. S.; Reghukumar, C.; Pathak, N.; Kadam, R. M. Experimental and theoretical approach to account for green luminescence from $Gd_2Zr_2O_7$ pyrochlore: exploring the site occupancy and origin of host-dopant energy transfer in $Gd_2Zr_2O_7$:Eu^{3+}. *RSC Adv.* **2016**, *6*, 44908−44920.
(63) Gupta, S. K.; Reghukumar, C.; Sudarshan, K.; Ghosh, P. S.; Pathak, N.; Kadam, R. M. Orange-red emitting $Gd_2Zr_2O_7$:Sm^{3+}: Structure-property correlation, optical properties and defect spectroscopy. *J. Phys. Chem. Solids* **2018**, *116*, 360−366.
(64) Gupta, S. K.; Ghosh, P. S.; Yadav, A. K.; Jha, S. N.; Bhattacharyya, D.; Kadam, R. M. Origin of Blue-Green Emission in α-$Zn_2P_2O_7$ and Local Structure of Ln^{3+} Ion in α-$Zn_2P_2O_7$: Ln^{3+} (Ln= Sm, Eu): Time-Resolved Photoluminescence, EXAFS, and DFT Measurements. *Inorg. Chem.* **2016**, *56*, 167−178.
(65) Gupta, S. K.; Ghosh, P. S.; Yadav, A. K.; Pathak, N.; Arya, A.; Jha, S. N.; Bhattacharyya, D.; Kadam, R. M. Luminescence Properties of $SrZrO_3$/Tb^{3+} Perovskite: Host-Dopant Energy-Transfer Dynamics and Local Structure of Tb^{3+}. *Inorg. Chem.* **2016**, *55*, 1728−1740.
(66) Gupta, S. K.; Mohapatra, M.; Godbole, S. V.; Natarajan, V. On the unusual photoluminescence of Eu^{3+} in α-$Zn_2P_2O_7$: a time resolved emission spectrometric and Judd−Ofelt study. *RSC Adv.* **2013**, *3*, 20046−20053.
(67) Gupta, S. K.; Sahu, M.; Krishnan, K.; Saxena, M. K.; Natarajan, V.; Godbole, S. V. Bluish white emitting Sr2CeO4 and red emitting Sr2CeO4:Eu3+ nanoparticles: optimization of synthesis parameters, characterization, energy transfer and photoluminescence. *J. Mater. Chem. C* **2013**, *1*, 7054−7063.
(68) Waetzig, G. R.; Horrocks, G. A.; Jude, J. W.; Villalpando, G. V.; Zuin, L.; Banerjee, S. Ligand-Mediated Control of Dopant Oxidation State and X-ray Excited Optical Luminescence in Eu-Doped LaOCl. *Inorg. Chem.* **2018**, *57*, 5842−5849.
(69) Zuniga, J. P.; Gupta, S. K.; Pokhrel, M.; Mao, Y. Exploring the optical properties of $La_2Hf_2O_7$:Pr^{3+} nanoparticles under UV and X-ray excitation for potential lighting and scintillating applications. *New J. Chem.* **2018**, *42*, 9381−9392.
(70) Gupta, S. K.; Sudarshan, K.; Ghosh, P. S.; Mukherjee, S.; Kadam, R. M. Doping-induced room temperature stabilization of metastable β-Ag_2WO_4 and origin of visible emission in α-and β-Ag_2WO_4: low temperature photoluminescence studies. *J. Phys. Chem. C* **2016**, *120*, 7265−7276.
(71) Su, B.; Xie, H.; Tan, Y.; Zhao, Y.; Yang, Q.; Zhang, S. Luminescent properties, energy transfer, and thermal stability of double perovskites La_2MgTiO_6:Sm^{3+}, Eu^{3+}. *J. Lumin.* **2018**, *204*, 457−463.

DOI: 10.1021/acsomega.8b03458
ACS Omega 2019, 4, 2779−2791